Numerical Simulation of Thick Line Width Measurements by Reflected Light

Gregory L. Wojcik, John Mould, Jr.
Weidlinger Associates, Los Altos, CA 94022

Robert J. Monteverde[†], Jaroslav J. Prochazka
VLSI Standards, Mt. View, CA 94943

John R. Frank, Jr.
SEMATECH, Austin, TX 78741

ABSTRACT

IC fabrication problems grow as nominal feature sizes shrink, due in large part to fundamental optical diffraction limits. Currently, one of the most pressing needs is robust critical dimension measurement. However, optical methods must be refined for this scale of submicron metrology, particularly in the case of thick features. This paper examines the problem of reflected light microscopy for nominal 1 micron high lines on silicon using 2-D, time-domain finite element simulations. The experimental basis is a prototype line width standard that is characterized using optical, contact, and SEM measurements. Microscope and simulated images are compared for 1 and 3 micron wide lines. Good "1st order" correlation is found between real and synthetic images but model uncertainties need to be reduced and microscope aberrations need to be quantified before "2nd order" differences can be eliminated. Numerical experiments are used to: relate images to resonance patterns in the feature; determine the strength of evanescent waves near the line; and contrast isolated and periodic line images as a function of pitch.

1. INTRODUCTION

Each new generation of integrated circuit technology achieves an increase in device density by fractionally reducing feature size. Today nominal IC features are under one micron and will be one-half micron in the near future. However, as characteristic dimensions have shrunk, fabrication and quality control problems have grown substantially. In large part this is because the optical wavelengths used in processing and inspection are 1/2 to 1/3 of the feature size, hence fundamental diffraction limits are being approached. Such limits reduce our degree of confidence in the proper corrective action needed to resolve these fabrication and quality control problems. Part of the short-term solution is more robust process monitoring by on-line critical dimension (CD) measurement.

Optical metrology may continue to provide an effective basis for CD measurement, but, the resolution limit of conventional optics and complex proximity effects raise serious questions about submicron accuracy. This is especially true for thick lines, i.e., those with comparable height, width, and illumination wavelength. Accuracy capabilities must be established and useful thresholding and calibration (correlation) criteria devised if optical metrology is to remain viable and complement alternative techniques like scanning electron microscopy. This paper examines the problem of accurate thick line measurement by comparing numerical simulation, optical imaging, and SEM imaging of a prototype calibration standard manufactured by VLSI Standards, Inc. Calibration of existing systems by means of a reliable thick line/substrate standard (comparator) is a first step towards enhanced optical accuracy.

By way of background, various forms of microscopy currently dominate modern IC metrology. Conventional imaging by visible light has been the mainstay and is still common by virtue of noninvasive operation, high throughput, and the large installed equipment base. Enhancements like confocal and coherence probe methods are attempting to extend functionality. Despite technical complexities, scanning electron microscopy (SEM) is now a practical alternative by virtue of lower voltages and full automation. More exotic scanning probe methods exist and show promise, but are currently of limited utility for general features. Electrical test probes provide an alternative to microscopy, albeit for cross-sectional area of dedicated conducting structures rather than dimensional images of arbitrary features.

[†] Now at KLA Instruments Corp., Santa Clara, CA 95052

Considering the breadth of technologies available for submicron metrology, it is clear that optics will face stiff competition in the future, particularly as SEM methods are made more efficient. The question is whether optical microscopy will eventually be dedicated to overlay measurements only, or limited to larger CDs (e.g., >0.7 microns), or whether enhancements will allow it to maintain some metrology utility in conjunction with other technologies. The issue comes down to that of accuracy, i.e., on the ability of future optical systems to provide absolute dimensional measurements of submicron features. The answer is in the hands of instrument makers and probably depends on their ability to incorporate complete and practical phase information into a *complex* image of the object, rather than merely offering intensity images at a reduced wavelength or with greater depth of focus.

To determine whether optical enhancements are indeed practical, renewed attention to the effective use of optical microscopy is called for, particularly with regards to measurements of thick lines and features on topographically complex substrates. Such research is very difficult to perform experimentally because of object size and the requisite parameter variations, as well as sundry uncertainties in fabricated geometry and optical system aberrations. On the other hand, numerical simulation, i.e., modeling and analysis, provides a practical way to investigate the problem. Numerical experiments can fully account for the vector wave nature of light while accommodating multi-dimensional model geometries, and the resulting optical resonances and edge effects that complicate today's imaging.

Although analysis by some form of numerical simulation is not new in optics, it has only been applied to metrology over the last decade. Some of the first work was done by Nyyssonen and coworkers, e.g., [1], [2], and more recently by Yuan and Strojwas [3], utilizing the so-called waveguide model of periodic diffractors to simulate scattering from 2-D structures. An alternative to this semi-analytical approach is a discrete numerical algorithm like the finite difference or finite element method in either the frequency- or time-domain. Discrete time-domain codes were successfully applied by Wojcik, et al. [4] to submicron particulate scattering problems associated with IC surface contamination and sensor calibration. These methods are new to optics but have proven their worth in other branches of engineering and applied physics, and offer a robust alternative that is relatively unfettered by geometrical constraints. Using either formal or informal inversion techniques they provide a means to actually verify feature cross-sections from image data.

Discrete numerical algorithms offer the advantage of geometric generality but with the disadvantage of requiring extensive number crunching. Fortunately, current workstations make all but the most computationally intensive algorithms practical. For example, calculations that had to be done remotely on a Cray 2 in 1987 for reasons of speed and memory can now be done on the newest IBM or Sun workstations with better overall turnaround time (calculation and post-processing time). The calculated images and scattering pictures described below take only fifteen minutes to execute and display on an IBM RS 6000, and this time is easily reduced to a couple of minutes if only microscope images are simulated.

In this paper we explore a conventional reflected light microscopy problem on the basis of 2-D, time-domain finite element simulations. We characterize the sample using physical, optical, and SEM measurements and critically compare simulated and microscope images. Numerical experiments are performed to: show what a microscope actually "sees" in terms of optical resonance patterns in the feature; determine the significance of evanescent waves; and compare isolated versus periodic models. This exercise provides a number of interesting insights into the problem of imaging and measuring thick features optically and may suggest some of the directions and ground rules for future research and development.

2. THICK LINE SAMPLE AND IMAGING SYSTEM

Measurements are made on a thick-line calibration die developed by VLSI Standards. Except for film thickness, the die is very similar to that described in [5]. The patterns are oxynitride on bare silicon and include lines, spaces, and pitches. The oxynitride is constituted to mimic the optical properties of photoresist but with better material stability. The lines have a nominal height of one micron and vary from one to five microns wide. At a wavelength of 0.546 microns, real parts of the refractive indices are approximately 1.64 for the oxynitride and 4.1 for the silicon.

The measurement system consists of a tuned, bright field optical microscope for reflected light, modeled after a prototype instrument at NIST described by Nyyssonen [6]. Tuning includes realigned

optical elements, a stabilized platform, and piezoelectric replacing mechanical focusing. Illumination is essentially monochromatic at a wavelength of 0.546 microns (green light), provided by a narrowband interference filter (0.019 micron bandwidth) and mercury arc lamp. Illumination at the object exhibits high spatial coherence by virtue of a small condenser aperture, yielding a coherence factor of 0.2 (= condenser NA/objective NA). The numerical aperture of the imaging objective is 0.95. Polarization is controlled by a linear polarizing element in the illumination optics.

The image is an intensity scan across the line feature obtained by illuminating a photomultiplier tube through a scanning slit in the image plane. The slit integrates a 0.156 micron wide swath in the object plane. A typical suite of measurements includes images at various levels of focus. The rule of thumb for best focus is the level that produces sharpest contrast, i.e., highest gradient between maximum and minimum intensities near the "edge" of the feature. The quantitative criterion for choosing the "best focus" level is the one that minimizes distance between the principal maxima in the image. Image crossplots from the 1 and 3 micron lines for TE (s-), TM (p-), and random (s + p) polarization are shown in Figure 1. Theoretically, the random polarization image should be a simple average of the TE and TM images, e.g., [7].

An important aspect of the optical imaging system is its relative simplicity and modelability. This facilitates comparisons between real and simulated (synthetic) images, and the actual feature. It is critical in this paper to have a deterministic system as a control so that images can be calculated with reliable fidelity from numerical simulations. Note that the underlying assumption here is that once the line width has been calibrated by the control optical system, the CD standard can then be used to calibrate the broadband optical systems commonly available in industry, which are typically more difficult to model than our control system. However, to use the standard as an effective comparator, simulation is required to account for nuances in feature and substrate properties, and to insure correct interpretation of results.

3. THE NUMERICAL MODEL

The numerical simulations are based on a rigorous finite element formulation of Maxwell's equations in the time-domain over a small region around and including the scattering feature, i.e., the finite element model. This model consists of a set of ordinary differential equations in time that result from the finite element semi-discretization of the spatial differential operator. Strong similarities exist between this approach and the finite difference method, e.g., [8]. An introductory description and comparison of the techniques may be found in [4], although the current codes are much enhanced and optimized versions of those described. A more comprehensive description of the Galerkin finite element formulation used here is available in [9].

The system of ordinary differential equations representing Maxwell's equations is integrated forward in time explicitly using a computationally efficient element-by-element algorithm. This approach eliminates the need to solve large implicit systems of linear equations but requires a time step smaller than the shortest wave transit time across any element. We have found by comparison that such explicit solutions are faster by nearly on order of magnitude than frequency domain solutions, and often require much less storage. The relative efficiency for 3-D problems is higher and in fact this time-domain algorithm is currently the only approach that makes 3-D modeling feasible on a routine basis.

Only steady-state solutions of Maxwell's equations are of interest for imaging. Using the time-domain approach, one choice is to integrate the system to steady-state assuming a transient startup with zero initial conditions. An alternative is to initialize the model to the free-field steady-state solution (i.e., without the scatterer) and then integrate the full system to steady-state from that point. This latter approach is used here in order to optimize boundary conditions. The free-field solution is obtained from an auxiliary analytical solution of the finite element equations for the actual boundary discretization. Because the free-field initial conditions are inconsistent with the presence of the feature, at start-up the full model produces a scattered field spreading directly from the feature and incident on the model's exterior boundaries. An efficient radiation boundary condition based on unidirectional wave motion (paraxial approximation) removes the scattered field there while simultaneously applying the steady incident field.

The numerical model is designed to propagate waves with negligible grid dispersion and domain truncation errors. The model used for virtually all of the calculations presented here consists of a grid 12.0 microns wide and 3.3 microns high partitioned into 720x226 elements as shown in Figure 2. Elements in the air and oxynitride are approximately 17 nanometers square. The silicon is represented by the lowest 0.32 microns of elements. The region around the scattering feature is modeled by skewed elements in the figure but generally only rectangular or stairstep approximations of the feature are considered in our calculations. The various numerical errors have been quantified by comparing finite element and exact solutions of Mie-type scattering problems for cylinders in free space. Very good agreement is obtained provided 15 or more elements support the illumination wavelength. The evanescent waves caused by diffraction from sharp edges have also been calculated and compared to results from a new theory of vector wave diffraction [10]. Agreement with the vector theory is excellent and it should be noted that no edge singularities are supported in the electric field for the TE polarized illumination considered here.

The electromagnetic field approximating the partially coherent, monochromatic incident light is composed of incoherent plane waves filling the symmetric cone of illumination. Only 2-D models are considered and cylindrical rather than conical illumination is assumed. For a coherence factor of 0.2, 3 and 5 waves in the plane of incidence yield nearly identical results so only 3 are used. The adequacy of this assumption will be considered later in the paper. The superposition of waves is essentially an integration, hence the incidence angles are located at the Gauss points (0°, ±8.5°) of the cone's angular interval and weighted accordingly, rather than evenly distributed with equal weights.

The numerical solution is complete when steady-state is achieved on a plane just above the feature. The resulting field is converted to an image by means of scalar Fourier optics. Functional details of the imaging optics, to the extent known, are included in the optical transfer function. Important degrees of freedom of the imaging model include illumination coherence factor, defocus, numerical aperture, polarization, spherical aberration, and comatic aberration. All but spherical aberration and coma are known for the system.

4. PHYSICAL MODEL CONSTRAINTS

There are many control parameters in the thick line imaging problem, each with its own measurement uncertainty and influence on the image. It is essential to begin the calibration process with the principal model and microscope parameters well-constrained, so as to minimize dimension of the space that must be sampled. Our efforts have concentrated solely on line parameters. Imaging parameters, particularly microscope aberrations and limitations of scalar imaging theory, need to be quantified in follow-on research. A future goal is to develop a generic rule table of imaging parameters, to be customized by users for different microscopes.

We initially constrain refractive index and line height using ellipsometry and profilometry at sites on the oxynitride film or margins surrounding the plasma etched patterns on bare silicon. Film thickness is further constrained by measurements of relative reflectivity and phase shift between bare silicon and the oxynitride film. These are the baseline measurements made by VLSI Standards in conjunction with optical imaging. Subsequent to optical imaging the sample was measured at SEMATECH using SEM images for width/pitch determination and profilometry for oxynitride film thickness.

For the sample considered, ellipsometry gives a refractive index of 1.63 in the oxynitride film at the microscope's illumination wavelength of 0.546 microns. Initial thickness measurements by the VLSI profilometer yield a film height of 0.979±0.003 microns. Calculations of relative reflectivity and phase shift for the film on silicon show that the measured values, 0.69±0.02 and 119°±4° respectively, are satisfied by a height of 0.966 microns. This is 1.33% thinner than the profilometer thickness and may be due to over-etching of the silicon, which would imply that the lines sit on a 0.013 micron silicon pedestal. Subsequent height measurements by a profilometer at SEMATECH gave a line thickness of 0.97±0.002 microns, which argues against a significant pedestal.

The above measurements are essentially nondestructive. Using SEM imaging to further constrain line geometry requires destructive preparation of the sample. This involves a coating of gold for line width determination, and focused ion beam (FIB) milling to expose cross-sections for shape characterization. SEM images of the nominal 1 and 3 micron lines and 4 micron pitch array are shown in Figure 3a,b,c. The first

two top-down views on the left indicate a uniform line width measured by the SEM's edge detection algorithm at 1.53 and 3.19 microns for the nominal 1 and 3 micron lines, respectively. The line's cross-section is exposed by FIB milling. Because the sample is mounted on a thick quartz substrate for handling, end-on views of the line cross-sections could not be obtained. Instead the sample was rotated to the extent possible, yielding off-axis views approximately 35° above the horizontal. These are shown on the right in the figure and indicate sides sloped about 8° from the vertical, with shape apparently uniform down the line. Note that the change from a smooth to rough surface near the milled edge is due to erosion of the gold coating by the FIB.

Since SEM images suffer their own set of uncertainties, they must be interpreted with care. In the case of the off-axis viewing arrangement, electron chromatic variations, the nonuniform collection field, and detector placement cause some illusory distortion of the features. These parallax effects are most pronounced in views of the periodic lines, Fig. 3c, which appear to widen away from the milled edge, in contrast to the uniform width indicated by the top-down view. To confirm the SEM cross-section, the focused ion beam was used to image the samples at the same off-axis arrangement. The heavier ions yield a relatively undistorted image (not shown) that indicates proportions and sideslope nearly identical to the SEM image cross-section.

In the case of the top-down views, the edge detection rule used by the SEM is only an approximation, particularly considering the significant side slope and gold coating. Therefore, accuracy of the SEM-measured line width is still difficult to assess, even to within 5%. Assuming profilometer thickness as the ruler, widths were also calculated from height-to-width proportions of the off-axis cross-sections. After accounting for the view angle, these only agreed to within 5% to 15% of the top-down measurements, and with no consistency from line to line. Pitch measurements generally gave much better agreement to optical measurement because they are relative rather than absolute.

5. REAL VERSUS SYNTHETIC IMAGES

We compare microscope and simulated images for our best guess at the thick line model, and illustrate the effects of certain parameters. This is a preliminary example of *numerical calibration*, essentially an ad hoc inversion process. It involves repeated trial and error variations on the target parameters in the numerical model until a best fit is achieved between measured and simulated images. The inversion can be made more rigorous as well as automated using least squares optimization and image sensitivity matrices (Jacobians).

Of the target parameters considered, primaries are width, sideslope, and defocus, and secondaries are spherical and comatic aberration. Since line height and refractive index are well-constrained by the measurements they are not used as target parameters in this paper, although measurement uncertainties certainly justify minor variations. The two features examined are the nominal 1 micron and 3 micron lines. We only consider synthetic and measured images for TE (s-) polarized illumination, i.e., electric field parallel to the line's axis, or equivalently, perpendicular to its cross-section (the plane of incidence). This is chosen because of its scalar simplicity, requiring one calculation per plane wave rather than the two necessary for random polarization (TE + TM). "Best focus" microscope images provide the basis for all comparisons. The image, in units of volts, is rescaled so that its specular intensity away from the edge is numerically equal to the reflectivity of silicon, and shifted horizontally to line up reasonably with the symmetric synthetic data.

5.1 Three Micron Line
Results for the 3 micron line are shown in Figure 4. The line cross-section is initially assumed to be rectangular rather than trapezoidal, with a refractive index of 1.63 and height of 0.966 microns. The minimum width that reasonably fits the measured image is 3.3 microns, shown against the data in Fig. 4a. Observe in this figure that the specular intensity (outer flat part of the image) is the reflectivity of bare silicon, the central plateau intensity is the reflectivity of a 0.966 oxynitride layer on silicon, and their ratio is 0.69, the measured relative reflectance. Existence of this central plateau indicates that at 3 micron spacing, and probably down to 2 microns, the edges are effectively isolated, i.e., their images do not interfere appreciably. Differences between real and synthetic images include the inner-maxima overshoot and shape of the outer-minima, namely, narrowness and overshoot. Changes in the synthetic image as line

width is increased from 3.3 to 3.4 microns are shown in the crossplot of Fig. 4b, where the primary effect is to substantially decrease the outer-maxima.

Effects of defocus are illustrated in Fig. 4c,d for the rectangular 3.3 and 3.4 micron lines. Levels of defocus that produced the greatest contrast between outer-maxima and -minima are found to be about -0.75 and -0.9 microns for the 3.3 and 3.4 micron lines respectively. This implies that "best focus" in the data actually represents a focus level close to the bottom of the line. Defocus is seen to decrease and broaden the outer-minima (with an inflection point near the minimum for 3.4 microns), increase the outer-maxima, either increase or decrease the inner-maxima, and consistently lower the central plateau (thus decreasing the apparent relative reflectance). If we were to pick a best fit to the data in terms of rectangular line width, it would be the 3.4 micron line based on the fit from outer-maxima to outer-minima.

Since the SEM images clearly indicate a trapezoidal rather than rectangular cross-section, we show the effect of 8° sideslope in Figure 4e,f. Based on measurements of the off-axis SEM view of the 3 micron line in Fig. 3, the model cross-section was assumed to have top and bottom widths of 3.19 and 3.48 microns, respectively. Comparing Fig. 4e to Fig. 4a,b for the rectangular 3.3 and 3.4 micron lines, we see strong similarities to the 3.3 micron line image despite the fact that the average width is 3.39 microns. With respect to the 3.3 micron rectangular line, the principal effect of slope is to slightly decrease the outer-maxima and enhance the inflection points. Applying -0.75 microns of defocus to the sloped image, Fig. 4f, shows stronger similarities to the defocused 3.3 micron image, Fig. 4c, but with reduced outer-maxima and inflections near the minima like the defocused 3.4 micron image, Fig. 4d.

5.2 One Micron Line
Results for the nominal 1 micron line are shown in Figure 5. As before, the cross-section is initially assumed to be rectangular with n = 1.63 and h = 0.966. Minimum width that fits the data is 1.3 microns, shown in Figure 5a. In contrast to the 3 micron line with its isolated edges, the 1 micron line exhibits a center maximum caused by edge interference. The obvious differences between synthetic and real images are shape of the minima and overshoot of the central maximum. Comparison of synthetic images as the width is increased to 1.4 microns is made in Fig. 5b, showing an increase in the central peak and inflection points in the minima.

Effects of defocus are shown in Figure 5c,d for the rectangular 1.3 and 1.4 micron lines. The greatest contrast between outer-maxima and outer-minima was found at -0.9 microns of defocus for both the 1.3 and 1.4 micron lines. Again, "best focus" in the data seems to represent a focus level near the silicon substrate. Defocus increases and narrows the maxima, broadens the minima and removes the inflection, and decreases the central maximum but introduces a pronounced local minimum there for the 1.4 micron line.

The effect of 8° sideslope is illustrated in Figure 5e,f. The model was assumed to have a top and bottom width of 1.22 and 1.55 microns, respectively, based on proportions of the off-horizontal SEM view in Fig. 3. Comparing the sloped and rectangular images, Fig. 5e to Fig. 5a,b, shows strong similarity to the 1.4 micron line with broadening of the outer-maxima and migration of the inflection points closer to the minima. Applying -0.9 microns of defocus to the sloped model eliminates the inflections near the minima and gives a better fit to data except for a slight oscillation in the central peak.

5.3 Aberration Effects
Besides defocus, the two optical aberrations considered in the imaging optics are spherical and comatic. Although we have no quantitative data on the actual aberrations of our microscope system, they are undoubtedly present and the wavefront distortions produced need to be included in our synthetic imaging. However, in the absence of real data, we can only estimate the relative order of effects on the image, particularly with respect to those caused by line width, side slope, and defocus.

Our basis for choosing reasonable amounts of aberration is a study by Kirk [11]. He concluded that the maximum amount of acceptable spherical aberration in a metrology objective should produce no more than - 1.5 wavelengths of wavefront distortion. Similarly, the maximum acceptable comatic aberration is 0.1 wavelengths. Since spherical aberration is even ordered and coma is odd ordered, their effects are symmetric and asymmetric, respectively. Here we only consider first order spherical aberration with no coupling to defocus.

Images distorted by spherical aberration are shown in Figure 6a,b for the two line widths. The 3.3 micron rectangular line image, Fig. 6a shows that the principal result is reduction of maxima, particularly the inner-maxima, with some migration of the inflection points and a slight rise in the central plateau. The sloped 1 micron image in Fig. 6b shows more significant effects. The central peak is reduced considerably while the outer-maxima are increased. There is also more oscillation of the signal indicating perhaps that 3 plane waves are not adequate to model partial coherence when spherical aberration is included. Note that these aberration effects are smaller but on the same order as those of size, shape, and defocus observed above. The point is that a reasonable amount of spherical aberration is sufficient to make the inner- or central maxima of the synthetic images approach those of the data.

Effects of comatic aberration were calculated but not shown. Coma causes asymmetry in the inner- and outer-maxima qualitatively like that observed in the data, but the amount of aberration assumed here is not sufficient to match the data. Other likely causes of observed asymmetry in the data are lens alignment and nonuniform illumination across the line. The latter has been quantified in images of the uniform substrate away from the patterned area but we have not attempted to model it in our calculations.

6. NUMERICAL EXPERIMENTS

Here we perform a series of numerical experiments to better understand the physics of thick line imaging. All parameters except for line dimensions are identical to those considered previously. These experiments begin by considering effects of varying the "model aperture" height on the image, which amounts to evaluating the significance of evanescent waves near the line. From there we perform calculations for a number of line widths and heights showing the scattered field in the coherent case and both coherent and partially coherent images using the scalar imaging algorithm mentioned above. Next we look at a sequence of periodic thick line models to see how coherent images of periodic features compare to coherent images of isolated feature.

6.1 Evanescent Waves

The electric field calculated at each node in the finite element grid includes both propagating and nonpropagating (evanescent) waves. When imaging the upwardly propagating numerical solution on some object plane (line) above the feature, it is necessary that the evanescent waves be negligible there, otherwise they will be converted to erroneous plane waves by the Fourier transform. To determine how close the object plane can be taken to the feature, the evanescent field strength must be evaluated. Herein lies one drawback of discrete numerical methods—the inability to directly separate wave types.

We did an indirect determination of evanescent wave strength by Fourier transforming the scattered and reflected field on 3 lines, at 0.0167, 1.0, and 2.0 microns above the feature, phase shifting the spatial spectrum on the higher lines back to the 0.0167 line, and imaging the 3 results. Since evanescent waves decay rapidly (exponentially) away from the feature's interface, with height in this case, image differences should likewise decay.

Figure 7 shows the experiment and results for 0.5 and 2.0 micron wide lines, both 1.0 micron high. The partially coherent images over the feature, say within ±3 microns on the scan, are almost identical indicating that evanescent waves are negligible as close as 0.03 wavelength (0.0167 microns) above the feature. Image differences apparent beyond ±3 microns on the scan are probably due to the scatter pattern's side lobes. These lobes curve up and cross the lines above the feature within the so-called model aperture, i.e., the model's horizontal extent, but the 2.0 micron line misses one. An examination of the spatial frequency spectrum on each line shows that the spectra are nearly identical except very near the objective's cutoff frequency (= NA/wavelength) where differences of approximately 15% are seen.

6.2 Synthetic Images

Results of numerical simulations for lines 1.0 micron high by 1.0, 1.25, and 1.5 microns wide and lines 1.0 micron wide by 0.500, 0.695, and 0.906 microns high are presented in Figures 8 and 9. All are for the case of TE (s-) polarized illumination. The top row of pictures in each figure shows phase of the scattered electric field. The middle row shows amplitude of the scattered field, all to the same gray scale. The scattered field is isolated by subtracting the one-dimensional free-field (incident and reflected) solution used for boundary and initial conditions from the total calculated field at each node in the model. Clearly, discontinuities in phase occur at the nulls or lows in the lobe pattern of the scattered field. These

field plots are for coherent illumination, i.e., a single plane wave, at normal incidence in the pictures shown. The bottom row shows synthetic partially coherent images obtained by superposing intensity images for 3 plane waves incident at 0.0° and ±8.5°.

It is interesting to note the correlation between standing waves within the feature and the lobe pattern of the scattered light. This suggests that the image for coherent illumination will be intimately related to details of the electromagnetic resonance patterns within the line. Also, since much of the interesting phase information is at fairly shallow angles, a relatively high NA objective is necessary to see it. However, most of this information is probably unavailable due to low side lobe intensity. The principal phase information is contained in the noncylindrical wavefronts at relatively low NA.

The bottom row of pictures shows scans over each line's synthetic image assuming partially coherent illumination (3 plane waves). The coherent image (1 plane wave) is overlayed for comparison and illustrates the smoothing effect of partial coherence. The addition of more plane waves to the partially coherent illumination provides additional smoothing outside the ±3 micron window but has negligible effect within. Although there is a fairly dramatic change in the scatter pattern as the line width or height changes, there is a relatively smooth transition between the partially coherent images. Note that the best indicator of line width in the partial coherence image is distance between the two primary minima.

The synthetic scans are made by imaging the upgoing scattered and reflected (i.e., total minus incident) fields on a line across the model one element (0.0167 microns) above the feature. Maxima and minima in the coherent image scans correlate one-to-one with maxima and minima seen in the scattered field across the top of the feature. Closer examination of the field just above the line shows that more subtle details in the image correlate as well, and relate to the line's interior resonance pattern. Observe that although the best measure of line width in the images is distance between the two primary minima, these correspond to field minima above the feature located approximately 1/5 of the line's width from each edge.

6.3 Periodic versus Isolated Lines

All of our attention in this paper has been on "isolated" thick lines. Despite this bias, periodic arrays of lines are important in CD metrology and deserve similar attention. To partially address the issue here we examine the relation between isolated and periodic line images as a function of pitch. This is especially relevant in the context of modeling since periodicity provides the mathematical underpinnings for many traditional algorithms, the waveguide model in particular, e.g., [1].

To this end we consider a periodic array of 1.0x1.0 micron lines separated by 2.0, 4.0 and 8.0 micron spaces (3, 5, and 9 micron pitches). Coherent images and scatter patterns are shown in Fig. 10. The pictures depict the scattered field from each line out to the periodic side boundary and start with the isolated line as reference field on top. Coherent images of the object plane (line) just above the feature are drawn over their period in the plot at the bottom of the figure. The periodic images show fair correlation with the isolated image at 5.0 micron pitch and good correlation at 9.0 micron pitch. Similarly, the scattered field patterns are recognizable for the 5.0 micron pitch and reasonably close at 9.0 micron pitch.

Observe that the scatter patterns within and near the line cross-section show much better correlation than the scattered field farther away. This observation suggests that better image correlation from periodic lines may be obtained by calculating the image from the field just outside the line and above the silicon interface instead of from the distorted field on the object plane. This can be done by using the Kirchhoff integral representation to extrapolate the electric field through free space onto an object plane, to which the imaging algorithm is applied.

7. CONCLUSIONS

These metrology simulations provide ample justification for the use of discrete numerical techniques. The results described are insightful and could not be obtained in a practical experimental fashion. They also suggest the utility of numerical models for exploring other IC optical issues, particularly in overlay. Modern workstations make this type of simulation a viable addition to the IC engineer's stock of analysis/research tools, and may ultimately be useful in a production environment.

The comparison section has shown that reasonable to good correlation can be obtained between experiments and simulations, but that discrepancies exist, some subtle and some not so subtle. The fact that the parameter variations considered did affect all salient features of the image implies that discrepancies are caused by uncertainties in characterizing either the model or the imaging optics, or the *scalar* transfer function assumed for the synthetic images. Once the system is adequately characterized, this work certainly suggests that image behavior is predictable by simulation.

There still remain some questions about "completeness" of the finite element modeling, particularly concerning 2-D approximations of 3-D phenomena. It is also clear that partially coherent imaging warrants further attention, specifically: the number of plane waves necessary and its dependence on factors like aberrations; and cheaper alternatives to incoherent superpositions of plane wave calculations, e.g., direct calculation of the coherence function.

In terms of using simulation to calibrate a line width standard, model and microscope uncertainties clearly need careful attention. Accurate calibration does not appear possible without good measures of microscope aberration, misalignment, and illumination nonuniformity. This is not to say that the microscope should be perfect, only that its quantitative behavior needs to be known. Conversely, simulations provide a means to rate the imaging tool's aberrations as well as establish absolute accuracy of both width and shape measurements.

Extensive numerical experiments like those above, but for general substrates, are necessary before we can make more comprehensive statements about optical metrology in the submicron realm. Modeling research, in conjunction with more formal inversion techniques, needs to be continued. The software reported here, in concert with modern workstations, will soon make such modeling accessible to engineers in the IC industry on a routine basis.

8. ACKNOWLEDGMENTS

9. REFERENCES

1. D. Nyyssonen, "Theory of optical edge detection and imaging of thick layers," *J. Opt. Soc. Am.*, 72(10), pp. 1425-1436, 1982.

2. C. P. Kirk and D. Nyyssonen, "Modeling the Optical Microscope Images of Thick Layers for the Purpose of Linewidth Measurement," *SPIE* Vol. 538, pp. 179-187, 1985.

3. C. Yuan and A. J. Strojwas, "Modeling of Optical Alignment and Metrology Schemes Used in Integrated Circuit Manufacturing," *SPIE* Vol 1264, pp. 203-218, 1990.

4. G. L. Wojcik, D. K. Vaughan, and L. K. Galbraith, "Calculation of Light Scatter from Structures on Silicon Surfaces," *SPIE* Vol. 774, pp. 21-31, 1987.

5. R. Monteverde and D. Nyyssonen, "A New Line Width Standard for Reflected Light Inspection," *SPIE* Vol. 921, pp. 395-405, 1988.

6. D. Nyyssonen, "Narrow-Angle Laser Scanning Microscope System for Linewidth Measurements on Wafers," National Institute of Standards and Technology Report NISTIR 88-3808, 1989.

7. M. Born and E. Wolf, *Principles of Optics*, Pergamon Press, New York, 1959.

8. K. S. Yee, "Numerical Solution of Initial Boundary Value Problems Involving Maxwell's Equations in Isotropic Media," *IEEE Trans. Antennas Prop.*, Vol. AP-14, pp. 302-307, 1966.

9. O. C. Zienkiewicz, The Finite Element Method, 3rd Edition, McGraw-Hill Book Co. Limited, 1977.

10. G. L. Wojcik and J. Mould, Jr., "A Mathematical Theory of Light Diffraction by Dielectric Wedges," Conference Proceedings, 5th Annual Review of Progress in Applied Computational Electromagnetics, Naval Postgraduate School, Monterey, CA, pp. 819-826, 1989.

11. C. P. Kirk, "A Study of the Instrumental Errors in Linewidth and Registration Measurements Made with an Optical Microscope," *SPIE* Vol. 775, 1987.
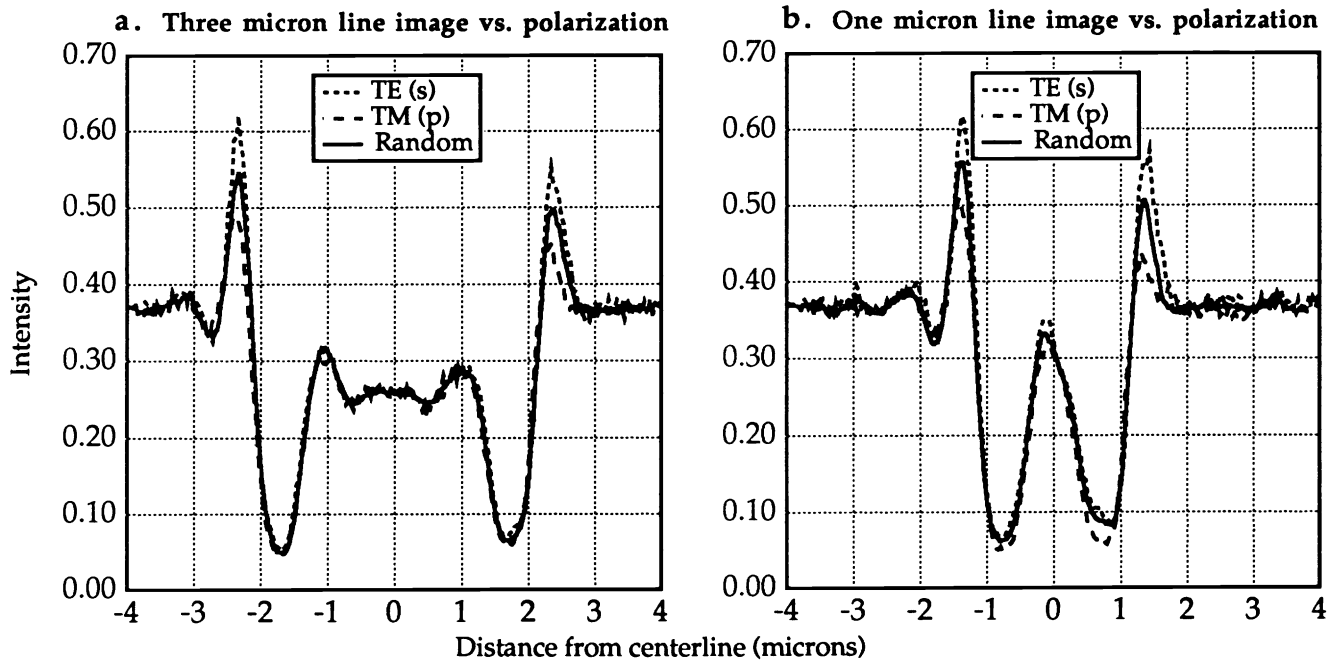
a. Three micron line image vs. polarization

b. One micron line image vs. polarization

Fig. 1. Images of the nominal three and one micron lines for three illumination polarizations. Theoretically, random should be average of TE and TM polarizations. All calculations and comparisons in the paper are done assuming TE polarization.
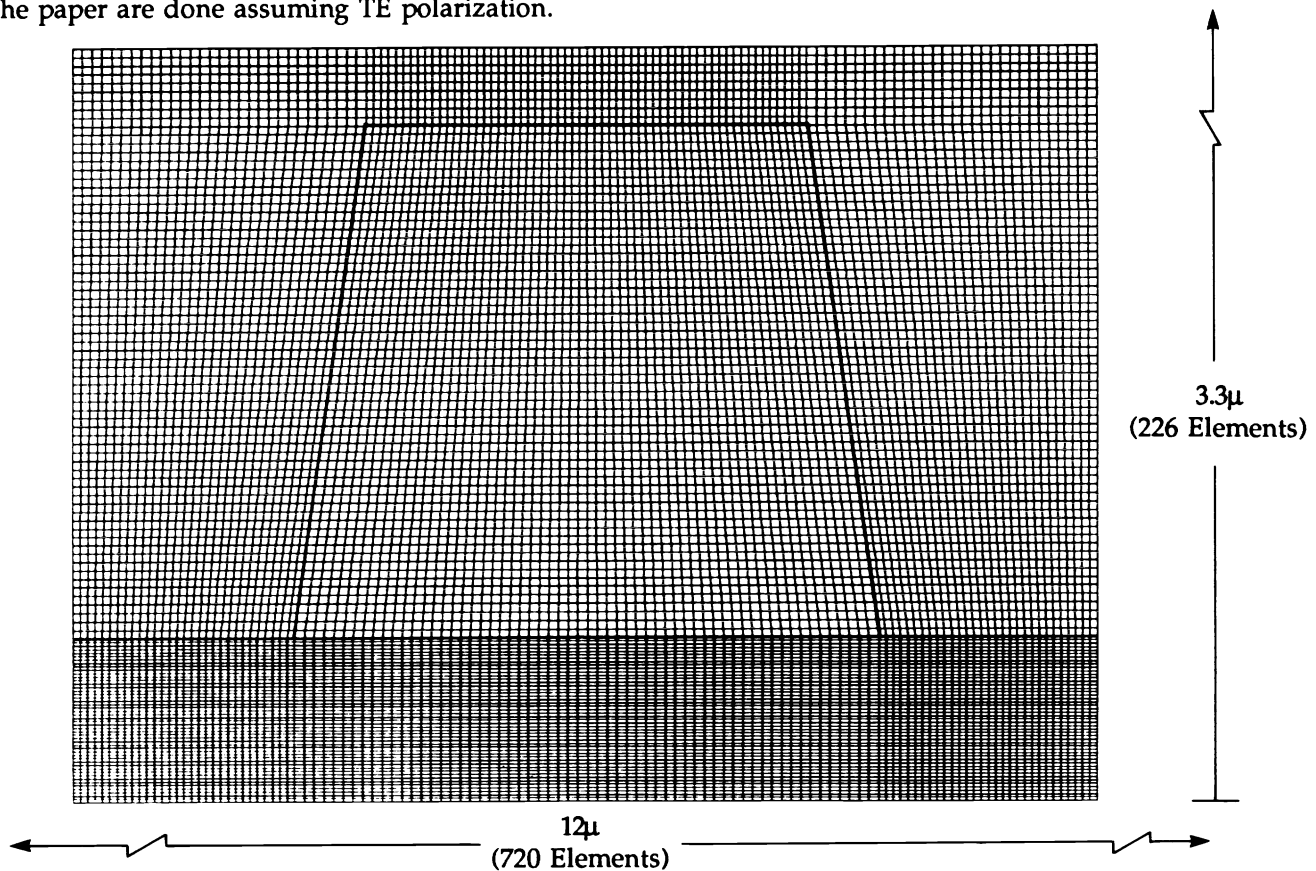

Fig. 2. A blowup of the finite element grid centered around the line cross-section, showing the level of discretization used. The line is 1.0 micron high and 1.0 micron wide at mid-height. The model extends 6.0 microns to the left and right of center and 3.3 microns above the bottom, continuing the same discretization.
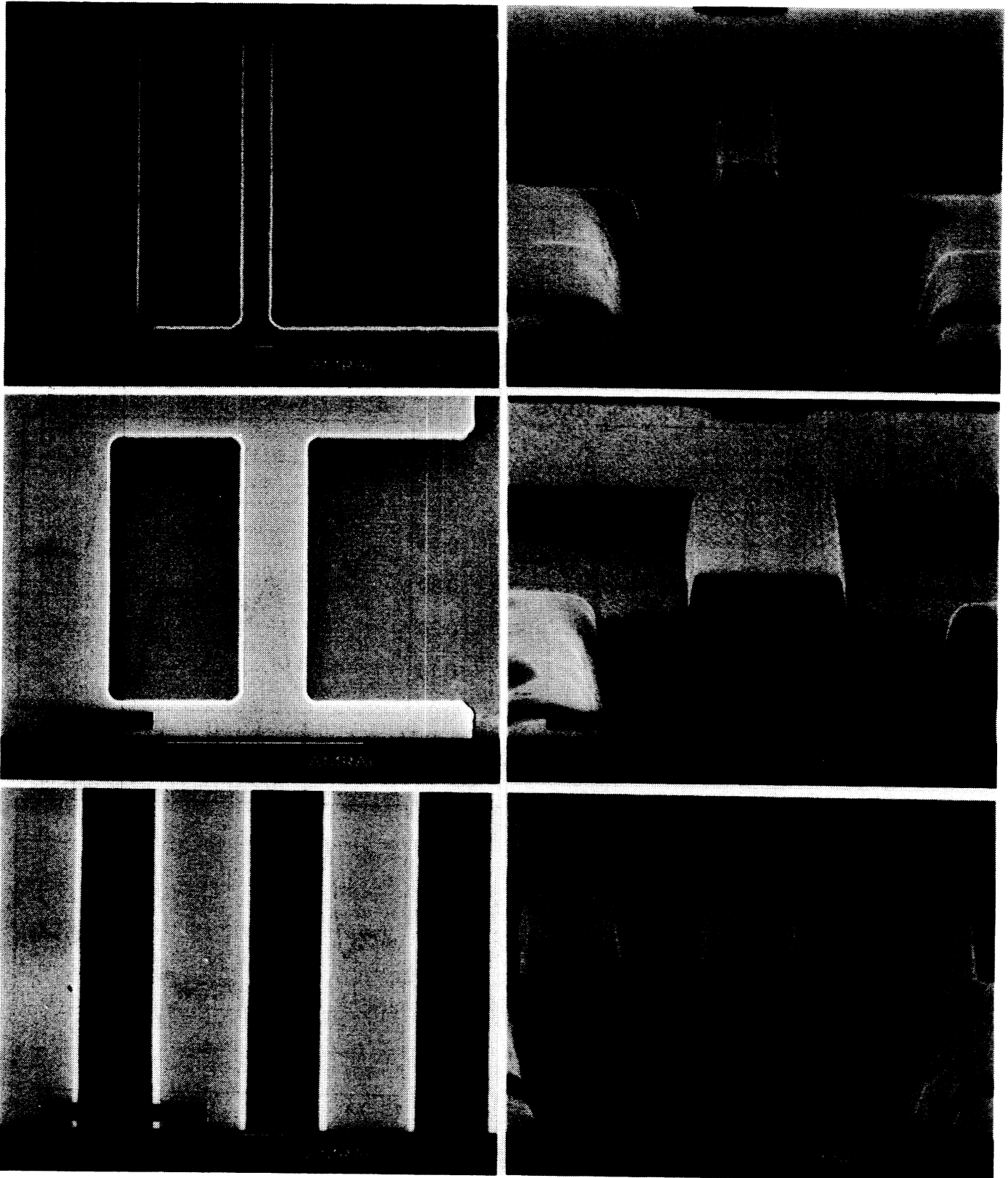
Fig. 3. Scanning electron microscope images of the VLSI Standards thick line die showing, from top to bottom, the nominal one micron line, the nominal three micron line, and the nominal four micron pitch. Top-down views used for line width measurement are shown on the left. Off-axis views for determination of cross-section shape are on the right. Focused ion beam milling is used to reveal the cross-section.
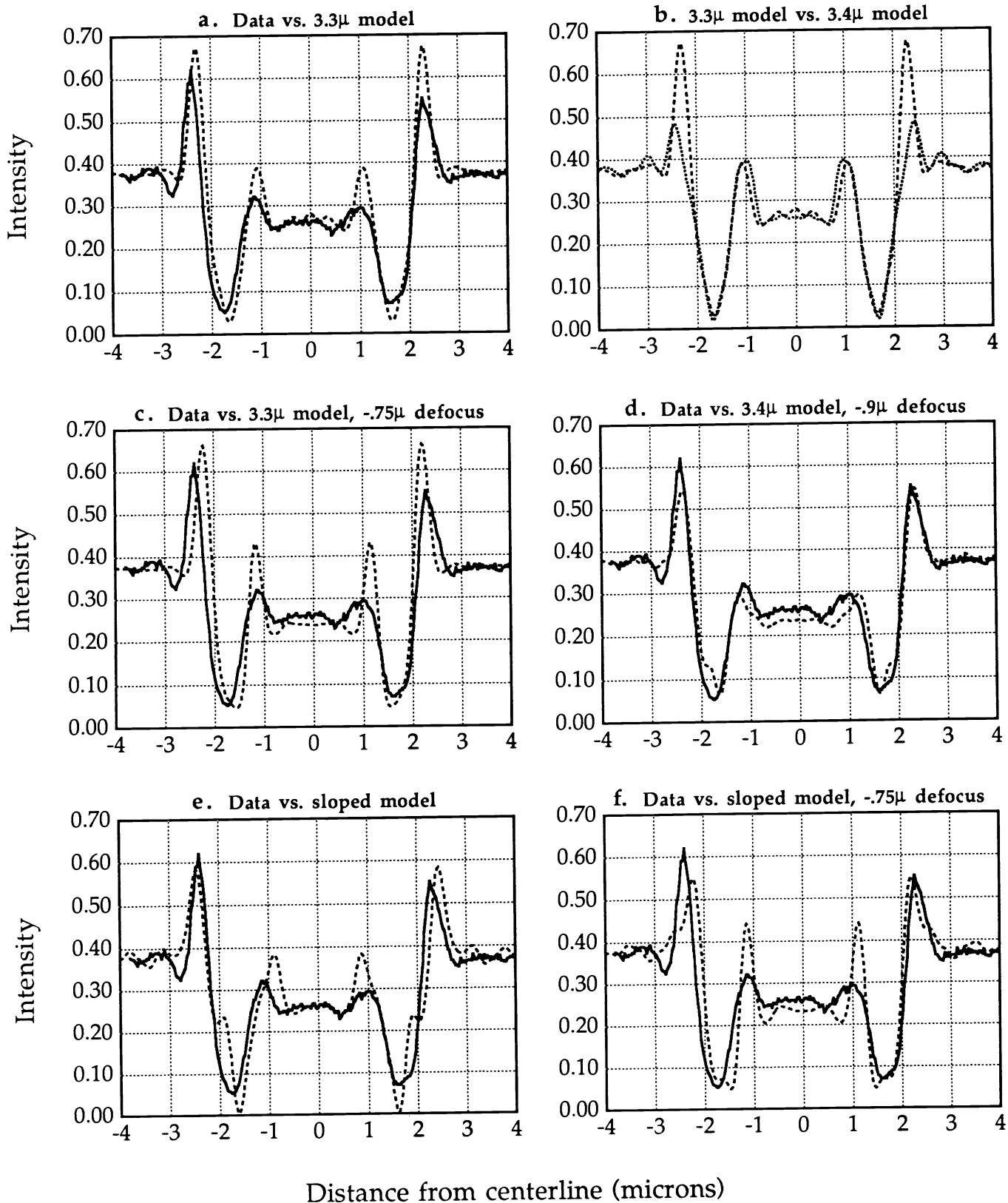
Fig. 4. Comparisons of the microscope images (solid) and the synthetic images (dashed) for the nominal *three* micron line. Plots show effect of width, defocus, and sideslope; see text for description.
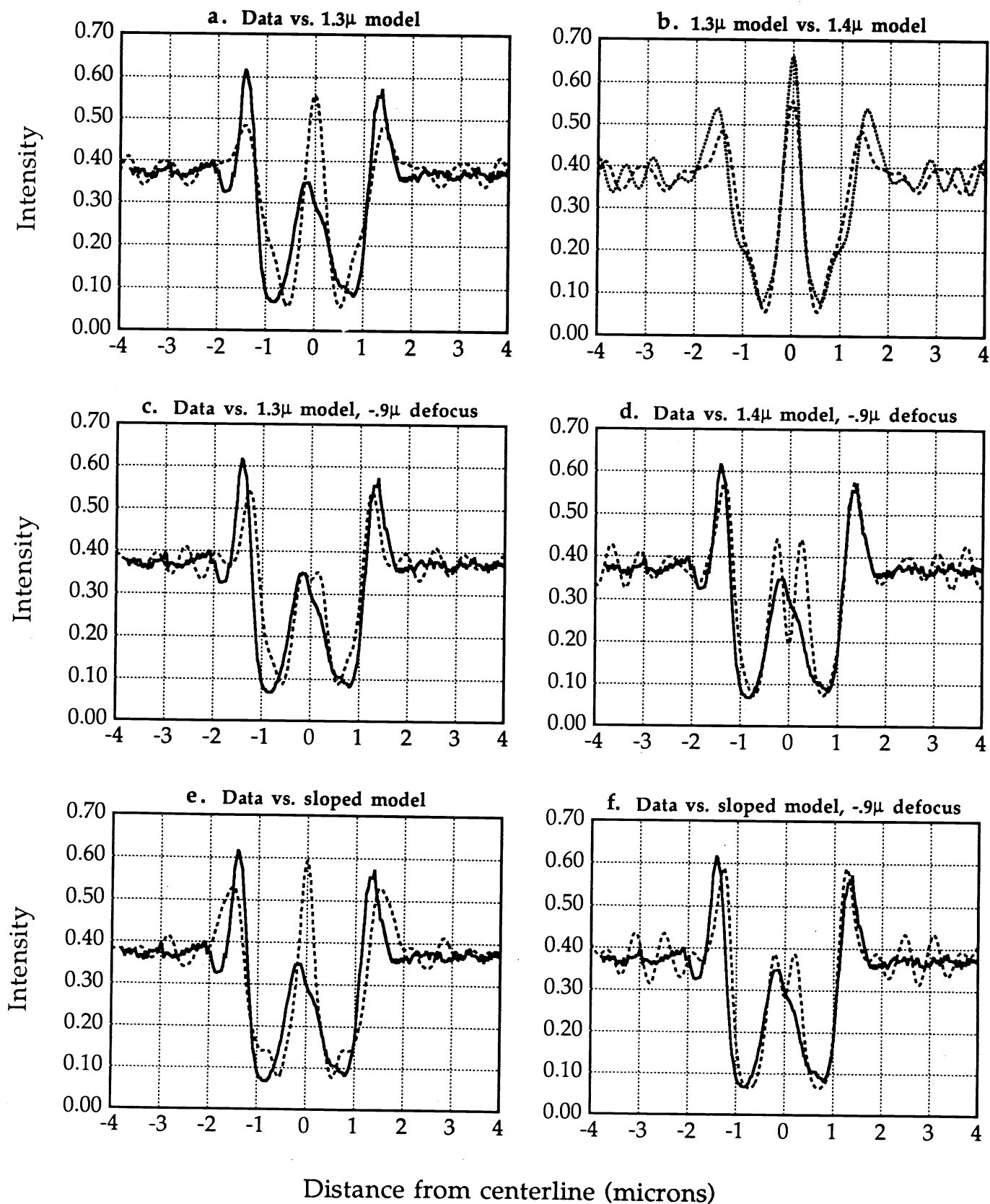
Fig. 5. Comparisons of the microscope images (solid) and the synthetic images (dashed) for the nominal *one* micron line. Plots show effect of width, defocus, and sideslope; see text for description.

a. Data vs. 3.3μ model, -1.5λ sph. aber.

b. Data vs. one μ sloped model, -1.5λ sph. aber.
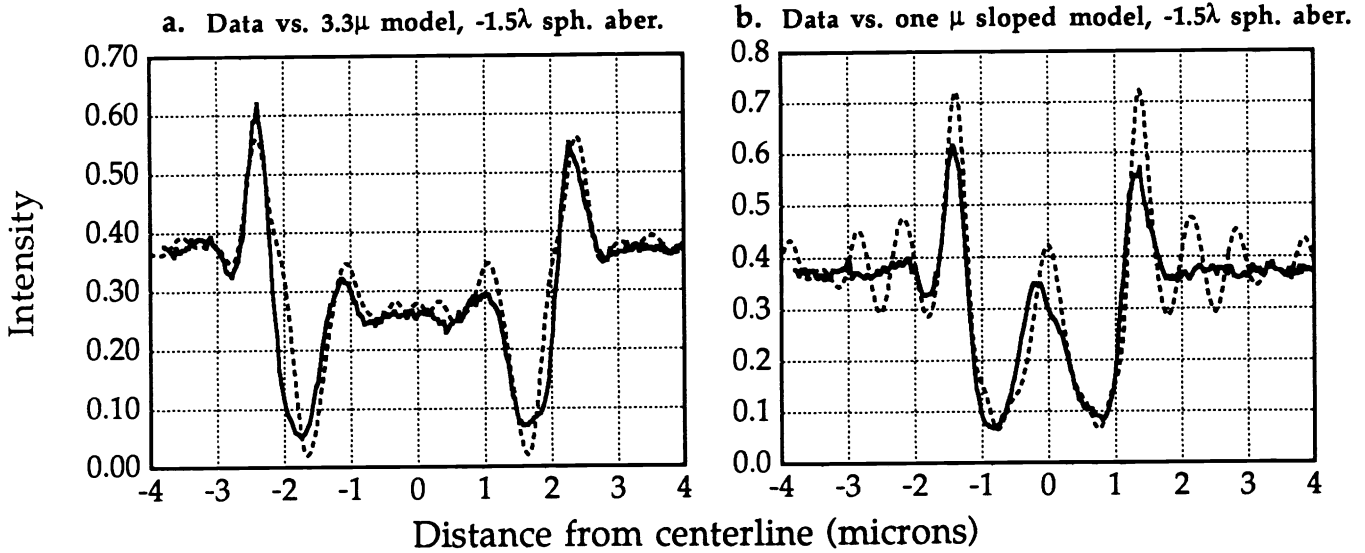
Fig. 6   Illustration of the effect of spherical aberration on the synthetic images (dashed) plotted against the microscope images (solid). Lines are the 3.3 micron rectangular model (left) and and the one micron sloped model (right).

a. 0.5μ wide, 1.0μ high line
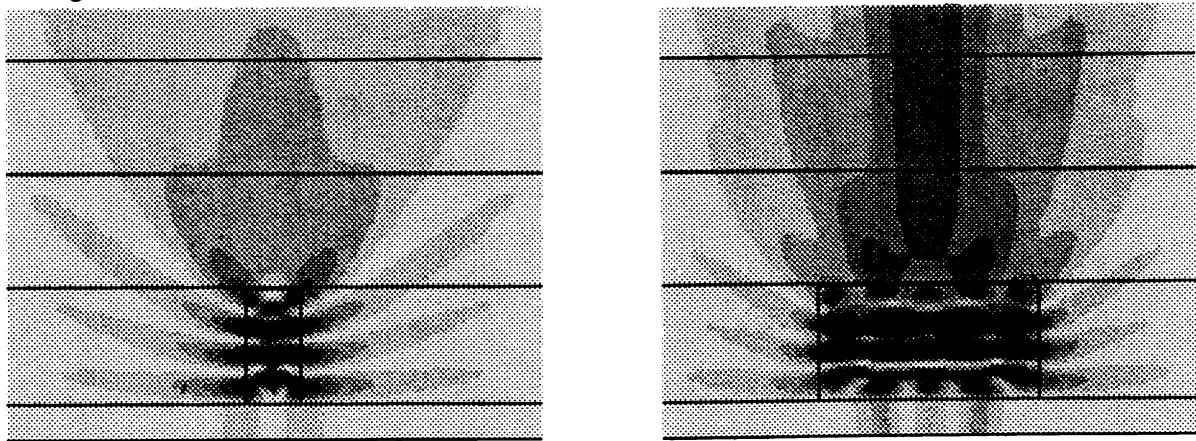
b. 2.0μ wide, 1.0μ high line
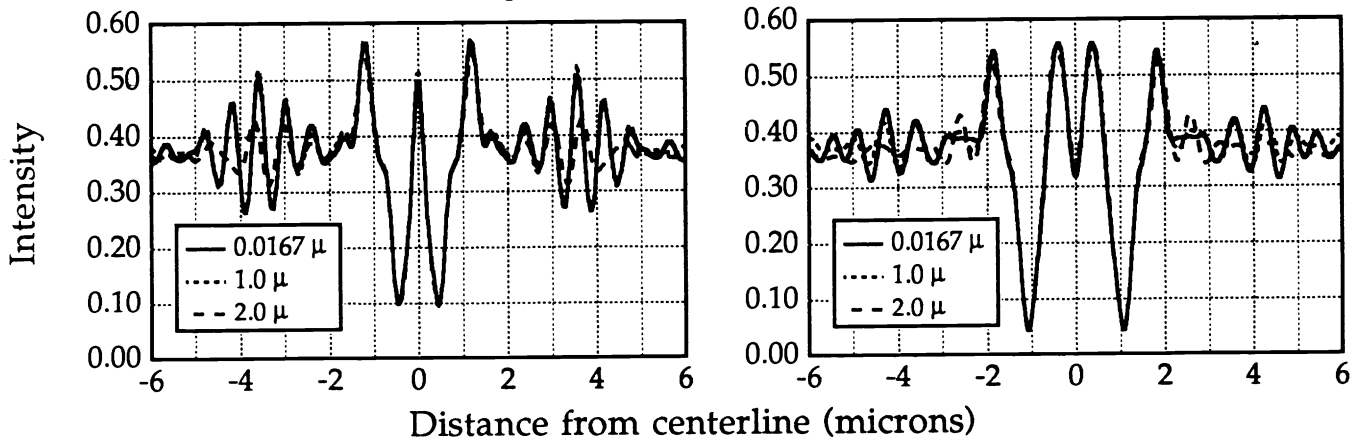
Fig 7.   Numerical experiment used to find the influence of evanescent waves on the image. The spatial spectrum is calculated on object lines 0.0167, 1.0, and 2.0 microns above the feature, extrapolated back to the closest line, and all three imaged. Since the images do not differ near the line, evanescent waves appear insignificant. Observed differences are due to the 2.0 micron object line missing near-horizontal lobes shown in scattering pictures above the images.
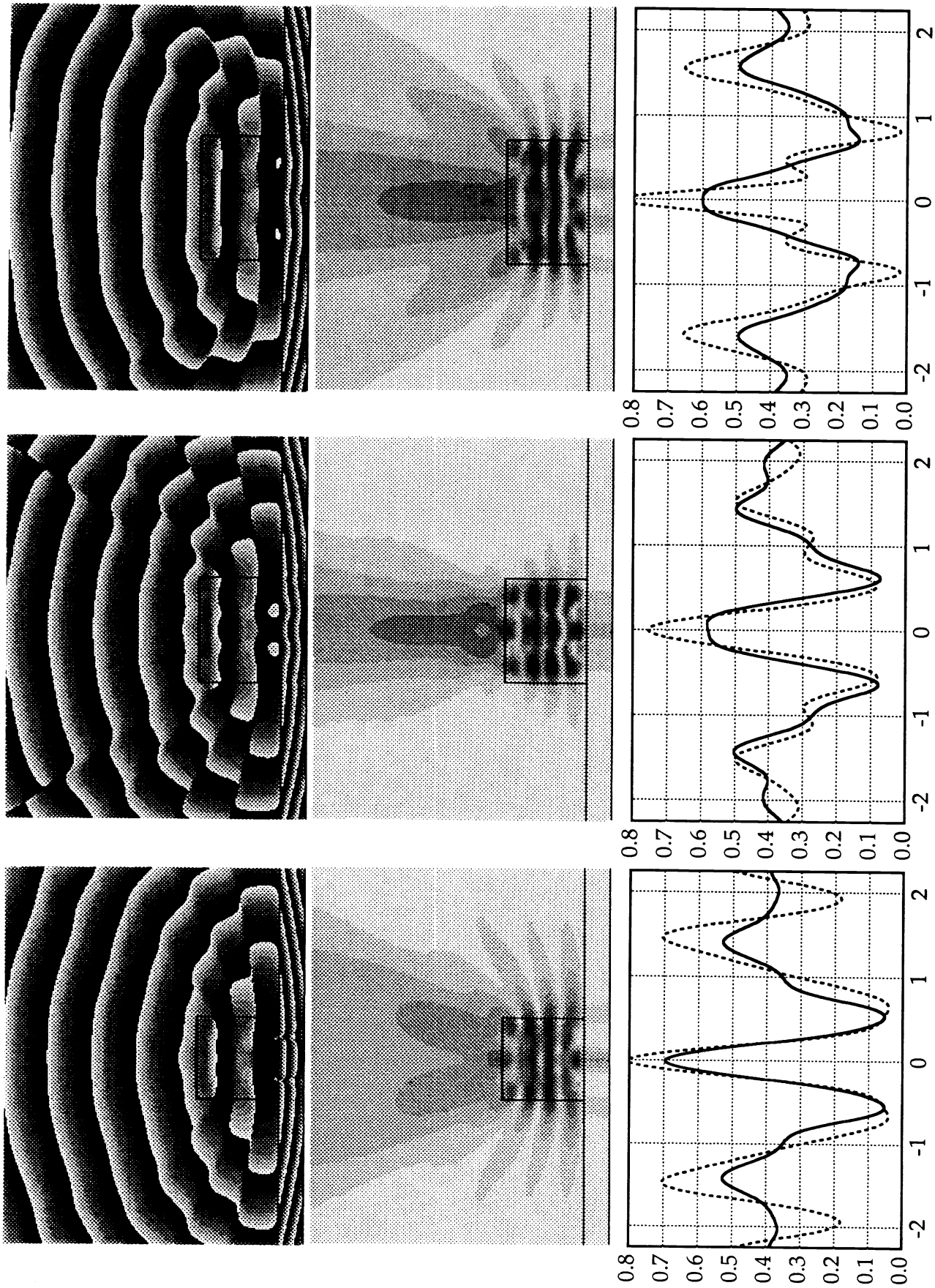
Fig. 8. Numerical simulations for lines 1.0 micron high by 1.0 (left), 1.25 (center), and 1.5 (right) microns wide. The top row shows phase of the scattered electric field, the middle row shows amplitude, and the bottom row shows reflected intensity images for both coherent (dashed) and partially coherent (solid) illumination. The horizontal scale, in microns, is the same for all.
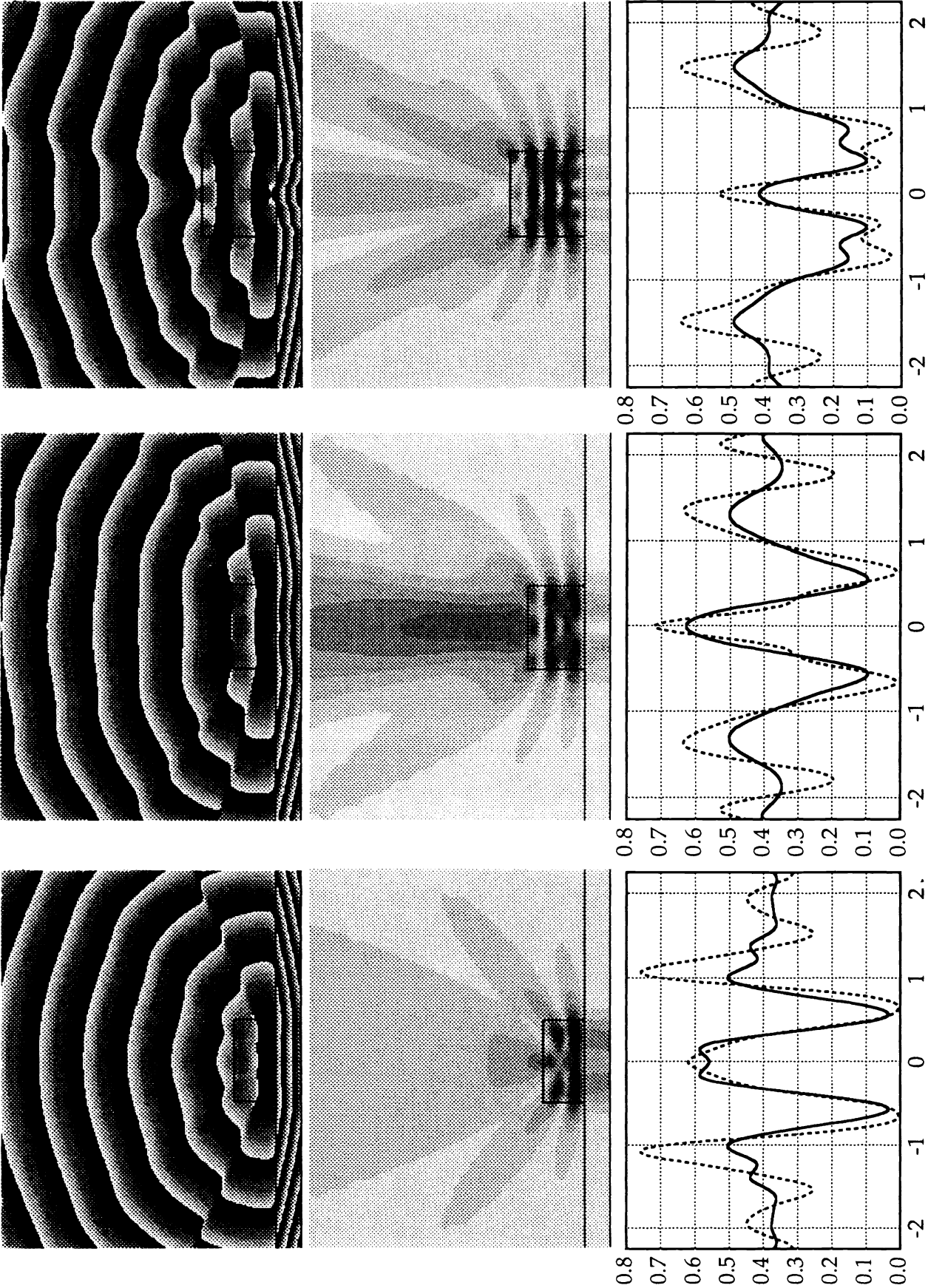
Fig. 9. Numerical simulations for lines 1.0 micron wide by 0.5 (left), 0.695 (center), and 0.906 (right) microns high. The top row shows phase of the scattered electric field, the middle row shows amplitude, and the bottom row shows reflected intensity images for both coherent (dashed) and partially coherent (solid) illumination. The horizontal scale, in microns, is the same for all.
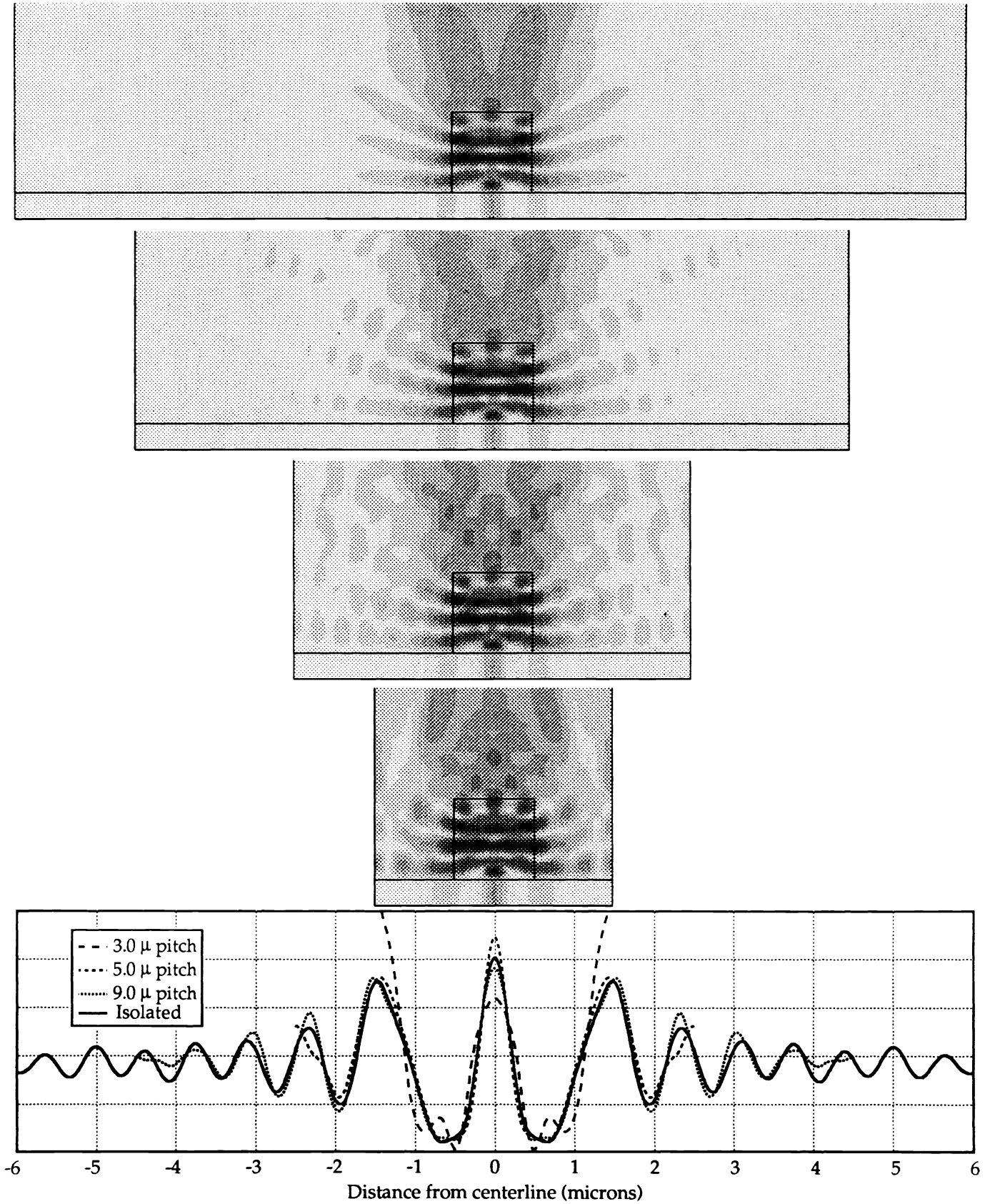
Fig. 10. Coherent scattering patterns and images for isolated and periodic 1.0x1.0 micron lines. Line pitches are ∞, 9.0, 5.0, and 3.0 microns respectively, starting from the top. Horizontal scale is in microns.